The Southern Ocean Momentum Balance: Evidence for Topographic Effects from Numerical Model Output and Altimeter Data

SARAH T. GILLE

Physical Oceanography Research Division, Scripps Institution of Oceanography, La Jolla, California

(Manuscript received 28 March 1996, in final form 14 April 1997)

ABSTRACT

The momentum balance of the Antarctic Circumpolar Current is investigated using both output from a high-resolution primitive equation model and sea surface height measurements from the Geosat altimeter. In the Semtner–Chervin general circulation model, run with approximately one-quarter degree resolution and time-varying ECMWF winds, topographic form stress is the dominant process balancing the surface wind forcing. Detailed examination of form stress in the model indicates that it is due to three large topographic obstructions located at Kerguelen Island, Campbell Plateau, and Drake Passage. The difference between wind stress and form stress represents the lateral transfer of momentum into and out of the ACC. It is examined both in zonal coordinates to conform to the model architecture and along mean streamlines in order to reduce the effects of standing eddies. In this particular model, in stream coordinates, biharmonic friction dominates the lateral transfer of momentum. Since biharmonic friction is a parameterization of subgrid-scale transient eddy processes, this indicates that the unresolved transient eddy processes play a critical role in fluxing momentum across the ACC in this model. Although the relative importance of individual terms in the momentum balance does not vary substantially along streamlines, elevated levels of eddy kinetic energy are associated with the three major topographic features. In contrast, altimeter data show elevated energy levels at many more topographic features of intermediate scales, suggesting that smaller topographic effects are better able to communicate with the surface in the real ocean than in the model.

1. Introduction

In the simplest approximation, the Southern Ocean resembles a continuous channel centered around the Antarctic continent; the force balances that generally describe the dynamics of closed basins, such as the North Atlantic, do not easily transfer to this region. In the momentum budget a strong zonal wind stress drives the eastward flowing Antarctic Circumpolar Current (ACC). No substantial continental boundaries are available to support western boundary currents to close the momentum balance, so what prevents the current from accelerating indefinitely? The physical processes that remove the momentum input by the wind and the resulting energetics of the ACC are the subject of this paper.

This study probes the dominant dynamical processes in the Southern Ocean by looking at the momentum balance in the quarter-degree version of the Semtner–Chervin primitive equation numerical model. Three specific issues are examined: If momentum is input by the wind, where is it removed from this numerical Southern Ocean? What processes carry momentum horizontally across the ACC? And to what extent are the results produced by the Semtner–Chervin model consistent with altimetric estimates of mean sea surface height and variability in the Southern Ocean developed by Gille (1994) and Gille and Kelly (1996)?

The momentum balance is considered in two coordinate systems, one zonal and the second along streamlines. Zonal coordinates are easily defined and conform well to the dominant zonal wind forcing in the Southern Ocean, while stream coordinates allow us to separate the processes specifically controlling the meandering ACC from those that predominate in the more quiescent regions outside of the circumpolar flow. Since the goals of this paper are to look at the processes governing the ACC itself, the analysis that follows will focus on the flow along ACC streamlines. In addition, in order to investigate the specific topographic features influencing the dynamics, this analysis will examine fluctuations of the momentum equation terms along streamlines. The results will show that the numerical model ACC undergoes substantial energy fluctuations along streamlines, but that the relative size of terms in the momentum balance does not change; therefore, eddy kinetic energy will be used to compare the model with altimeter data. Differences between surface eddy kinetic energy distributions measured by the altimeter and in the model

Corresponding author address: Dr. Sarah T. Gille, Physical Oceanography Research Division, Scripps Institution of Oceanography, La Jolla, CA 92093-0230.
E-mail: sgille@ucsd.edu

suggest that the model may not feel bottom topography as effectively as the ocean does.

2. Background: Processes balancing wind

In theoretical and modeling studies, oceanographers have long speculated about the dominant forces controlling the momentum balance of the ACC. Consider the zonal momentum equation, in this case formulated in spherical coordinates as it is used in the Semtner–Chervin model (Semtner 1986) and time averaged:

$$\frac{u_f - u_i}{\Delta t} + \frac{1}{a\cos\phi}\frac{\partial(\overline{u}\,\overline{u} + \overline{u'u'})}{\partial\lambda} + \frac{1}{a\cos\phi}\frac{\partial(\overline{v}\,\overline{u}\cos\phi + \overline{v'u'}\cos\phi)}{\partial\phi} + \frac{\partial(\overline{w}\,\overline{u})}{\partial z} + \frac{\partial\overline{w'u'}}{\partial z} - \frac{\overline{u}\,\overline{v}\tan\phi}{a} - \frac{\overline{u'v'}\tan\phi}{a} - f\overline{v} = -\frac{1}{\rho_0 a\cos\phi}\frac{\partial\overline{p}}{\partial\lambda} + \mu\overline{\frac{\partial^2 u}{\partial z^2}} + A_m\nabla^4\overline{u}. \quad (1)$$

Here overbars indicate time averages and primes indicate deviations from time averages. The terms u, v, and w represent zonal, meridional, and vertical velocity; f is the Coriolis parameter; λ and ϕ are longitude and latitude; a is the radius of the earth; ρ_0 is mean density; μ represents vertical viscosity; and A_m is the horizontal viscosity coefficient. The terms u_f and u_i represent final and initial velocities and Δt is the total time duration considered; these terms are used to estimate the velocity tendency. Equation (1) is Boussinesq and hydrostatic and uses the continuity equation $\nabla\cdot\mathbf{u} = 0$.

Geostrophy dominates the system: at any point throughout the ocean, the leading order balance in (1) is between the Coriolis term fv and the pressure gradient term $(\rho_0 a\cos\phi)^{-1}\partial p/\partial\lambda$. Momentum is input by the wind through the surface boundary condition. It is extracted via the pressure gradient term below the depth of the shallowest bathymetry, bottom friction (represented as a bottom stress in the vertical viscosity term), and through no-slip lateral boundary conditions at continents and topographic features. The other terms transfer momentum from wherever it enters at the surface to the boundaries where it is removed. Horizontal transfer occurs by biharmonic friction, $A_m\,\nabla^4 u$ (often referred to as viscosity or momentum diffusion), and by horizontal momentum flux (or Reynolds stress) divergences, $(a\cos\phi)^{-1}\partial(uu)/\partial\lambda$ and $(a\cos\phi)^{-1}\partial(v\,u\cos\phi)/\partial\phi$. Time averaging the momentum equation minimizes the time evolution term $(\partial u/\partial t)$ and allows us to compare the relative sizes of momentum flux divergences due to standing eddies, $(a\cos\phi)^{-1}\partial(\overline{u}\,\overline{u})/\partial\lambda$ and $(a\cos\phi)^{-1}\partial(\overline{v}\,\overline{u}\cos\phi)/\partial\phi$, with those due to transient eddies, $(a\cos\phi)^{-1}\partial\,\overline{u'u'}/\partial\lambda$ and $(a\cos\phi)^{-1}\partial(\overline{v'u'}\cos\phi)/\partial\phi$. Vertical transfer results from vertical eddy viscosity and from the vertical momentum flux divergence, $\partial(wu)/\partial z$. The small metric terms, $a^{-1}\overline{u}\,\overline{v}\tan\phi$ and $a^{-1}\overline{u'v'}\tan\phi$, are accelerations due to the curvature of the earth.

What physical processes actually counteract the substantial surface wind forcing in the Southern Ocean? In past studies, all of the terms in (1) have been considered in detail. Momentum input by the wind could conceivably be balanced by bottom friction; however Gill (1968) estimated that the frictional drag terms would need to be unrealistically large. Likewise, although one might imagine that the horizontal momentum flux divergence terms transfer momentum input by the wind to regions where it could be removed frictionally, observational evidence from current meters (Bryden and Heath 1985) and altimeter measurements (Morrow et al. 1992; Johnson et al. 1992) indicates that the horizontal momentum fluxes are too small to counteract wind forcing. In locations where the Reynolds stresses were statistically significant, they tended to be of the ''wrong'' sign, suggesting that the horizontal eddies drive the mean flow rather than dissipating it.

Since neither bottom friction nor horizontal friction can be sufficiently large, the leading candidate to balance wind stress is topographic form stress, which is associated with pressure gradients across bathymetric ridges. The idea was first proposed by Munk and Palmén (1951) who provided a physically intuitive description illustrating how the pressure exerted on the deep zonal flow by a meridional ridge could balance wind stress. Using a series of eddy-resolving two-layer quasigeostrophic numerical models, McWilliams et al. (1978) found that topographic form stress was an essential process limiting ACC transport. More recent numerical investigations have confirmed that the wind stress is balanced by form stress, rather than by frictional drag or momentum fluxes, both in a quasigeostrophic model (Wolff et al. 1991; Marshall et al. 1993) and in the Fine Resolution Antarctic Model (FRAM) (Killworth and Nanneh 1994; Ivchenko et al. 1996; Stevens and Ivchenko 1997). In this analysis of the Semtner–Chervin model output, form stress also emerges as the dominant process balancing wind stress.

As noted by Johnson and Bryden (1989), for a circumpolarly averaged path, form stress may be written:

$$\text{form stress} = -\oint\int_{-H(x)}^{0}\frac{1}{\rho_0}\frac{\partial\overline{p}}{\partial x}\,dz\,dx = -\oint\int_{-H(x)}^{0} f\overline{v}_g\,dz\,dx \quad (2)$$

using the standard geostrophic relationship, where v_g, the geostrophic velocity, is specifically the portion of the meridional velocity explained by the pressure gradient. Alternatively, noting that the total velocity is simply the sum of geostrophic and ageostrophic components so that $v = v_g + v_{ag}$ and that

$$-\oint \int_{-H(x)}^{0} f\overline{v}\, dz\, dx = 0$$

since there is no net flow into the Southern Ocean, (2) may also be written:

$$\text{form stress} = \oint \int_{-H}^{0} f\overline{v}_{ag}\, dz\, dx. \tag{3}$$

Note, however, that the above definitions of form stress, (2) and (3), apply only for averages along circumpolar paths; for noncircumpolar regions an additional pressure term will be introduced later.

In order for form stress to balance wind forcing exactly, momentum must transfer vertically, directly from surface to bottom. If form stress and wind forcing do not act in the same geographic locations, then horizontal momentum fluxes across the ACC will also be required to close the momentum balance. These lateral transfers will be considered in the discussions of the momentum balance, which follow. The next section describes the Semtner–Chervin model used to consider the ACC momentum balance in this study. Readers less interested in model mechanics may wish to skip ahead to the discussion of the momentum balance and energetics beginning in section 4.

3. Momentum information from model output

The Semtner–Chervin model is a 20-level global general circulation model based on the Cox–Bryan code (Semtner 1986). It solves the primitive equations represented by the unaveraged form of (1) in the zonal direction and its meridional counterpart, along with tracer conservation equations for temperature and salinity. For this study, results were analyzed from the ''quarter-degree'' version, which implemented several refinements from the earlier half-degree version (Semtner and Chervin 1992). A free sea surface was implemented based on the formulation by Killworth et al. (1991). The horizontal resolution was set to 0.4° in the zonal direction and 0.4° cos(ϕ) in the meridional direction so that square grid boxes are maintained and the horizontal resolution increases at higher latitudes. In the Southern Ocean, this marginally resolves typical eddy length scales: between 70° and 30°S the model resolution ranges from 15 to 38 km. For comparison, multiplying 2π times the first baroclinic Rossby radii calculated from hydrographic data (Houry et al. 1987) yields length scales between 30 and 120 km for the South Atlantic. Similarly, using Geosat altimeter data Gille and Kelly (1996) estimated the eddy decorrelation length scale in the Southern Ocean to be 85 km.

The model was initialized with the output from a 32.5-yr run of the half-degree model. At one-quarter degree resolution, it was then run for 1 yr using climatological winds. Finally, for the period from January 1986 to December 1989, it was forced with ECMWF operational forecast model winds (Trenberth et al. 1989). Surface buoyancy forcing was based on the Levitus (1982) monthly climatologies with a one-month relaxation timescale. Unlike older versions of the model, this version included no relaxation to Levitus climatology anywhere below 2000 m. Using a three-month timescale, temperature and salinity were relaxed to ''annual mean Levitus'' climatology only in the upper 2000 m within 7° of the northern and southern boundaries of the model domain (located at 65°N and 75°S, respectively) and within 7° of the Straits of Gibraltar (Semtner and Chervin 1992; A. Semtner 1994, personal communication).

The model is formulated on the Arakawa B-grid: temperature–salinity points are located at the center of model grid boxes; velocity points are on the corners at the same depth as temperature and salinity points. Boundary conditions are

$$\mu\frac{\partial u}{\partial z} = \frac{\tau^{\lambda}}{\rho_0} \tag{4}$$

at the surface, and

$$\mu\frac{\partial u}{\partial z} = bu\sqrt{u^2 + v^2} \tag{5}$$

at the bottom, where b, the bottom friction coefficient, is unitless and takes the value 1.225×10^{-3}. The horizontal viscosity, A_m, is $-11 \times 10^{19}\ \cos^2(\phi)\ \text{cm}^4\ \text{s}^{-1}$. No-slip boundary conditions are imposed on the side walls so that u and v are zero at all grid points corresponding to land.

Although the details of the resolution and forcing differ, the basic model formulation is the same as FRAM (FRAM Group 1991), and many of the results are qualitatively similar. While investigations of the mean momentum balance in FRAM (Killworth and Nanneh 1994; Ivchenko et al. 1996; Stevens and Ivchenko 1997) have averaged 72 instantaneous monthly model dumps, the Semtner–Chervin model output used for this study consists of time-averaged means, variances, and covariances of the model variables produced from three-day model snapshots. [Jayne and Tokmakian (1997) have pointed out that primitive equation models include significant inertial oscillations, which are often aliased by regular periodic sampling schemes; the frequent sampling of the Semtner–Chervin output is likely to reduce the magnitude of this aliased energy.] The impact of the nonlinear advective terms in the momentum balance may be examined by computing derivatives of the stored u, v, and w variance and covariance terms. This permits a reasonable approximation of all of the terms in the momentum balance.

Several subtleties in the model formulation imply that perfect estimates of these mean terms cannot be obtained, and the momentum balance will not close com-

pletely. Although the term $f\bar{v}$ may be determined exactly, the pressure gradient term

$$(\rho_0 a \cos\phi)^{-1}\partial\bar{p}/\partial\lambda$$

is not stored by the numerical model and must be calculated by applying the model equation of state to the mean temperature and salinity values. A partial correction for the nonlinearities in the equation of state is made using the standard deviations of temperature and salinity (Gille 1995) but it cannot be expected to account for all of the nonlinearities.

In addition, the vertical viscosity μ is Richardson number dependent (Pacanowski and Philander 1981) and thus is time dependent and highly nonlinear. In the deep ocean, μ is small and roughly constant at 1 cm^2 s^{-1}, but at shallower depths nonlinearities in μ may cause significant errors in the momentum balance. Since μ depends on covariances of vertical derivatives, which are not stored, its mean may not be corrected by using the variance. Thus the time mean of upper-ocean vertical viscosities cannot be calculated directly. Moreover, errors may have been incurred in recomputing the wind field used for the Semtner–Chervin runs. These errors in μ and wind forcing hinder upper-ocean analyses, but are not a problem in the results presented here.

Additional errors arise from several of the other terms in the momentum equations. In the model formulation, the nonlinear advective terms are computed by adding adjacent values and then multiplying and computing derivatives so that the time-averaged results involve not only the correlations $\overline{u'u'}$, $\overline{v'v'}$, and $\overline{u'v'}$, which are stored in the mean model output, but also the correlations of adjacent points (for example, $\overline{u'_{j,i+1}v'_{j,i}}$), which are nonnegligible and contribute to the misfit in the final results.

The vertical advective terms also play a significant role in the momentum balance. The vertical velocity w is computed at the same locations as u and v for dynamical computations, and at the same locations as T and S for tracer computations, but only the tracer computation value is stored. Differences between these values can be substantial, so in this analysis $\overline{w}$ is recomputed directly from u and v; however, the stored covariance terms $\overline{u'w'}$ and $\overline{v'w'}$ rely on w at T, S points so that the dynamical vertical advection terms cannot be determined exactly. Nonetheless, errors induced by these minor technical problems do not significantly affect the major terms in the momentum balance.

In the Southern Ocean, the model indicates the flow to be confined to two or more narrow jets, in general agreement with hydrographic observations (Orsi et al. 1995) and altimeter measurements (Gille 1994). The average transport through Drake Passage in the model output is 200×10^6 m^3 s^{-1}, which exceeds the observed value of 130×10^6 m^3 s^{-1} by about 50%. Although the model and observed transports are of similar magnitudes, the large discrepancy suggests that the model may not fully capture the physical conditions governing the ACC. In qualitative comparisons between the model output and observations, Stammer et al. (1996) found that the model represented some features of the large-scale circulation well but had shortcomings in duplicating other features. This study will specifically investigate Southern Ocean momentum, and the results of this analysis will provide a framework for examining altimeter data. The next sections will examine the critical dynamics in the model momentum balance.

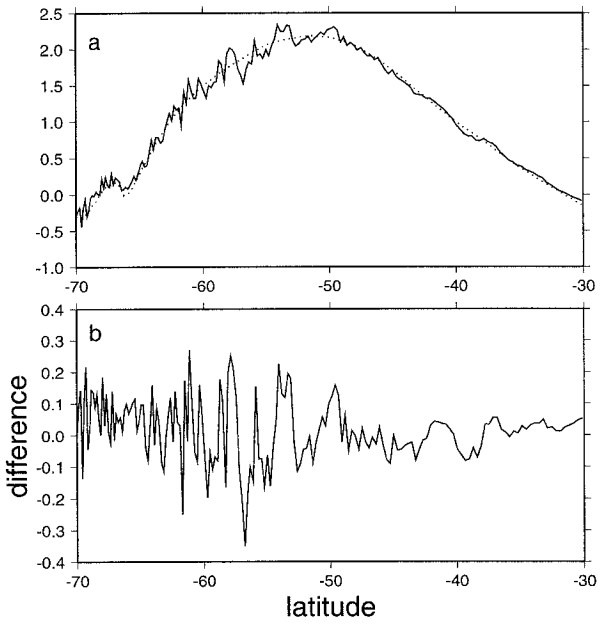

FIG. 1. Vertically integrated and zonally averaged dominant momentum balance in the quarter-degree Semtner–Chervin model output (in cm^2 s^{-2}). (a) The pressure gradient term $L^{-1}\iint \rho_0^{-1}\,\partial\overline{p}/\partial x\,dx\,dz$ (solid line), which is the negative form stress, and the integrated stress term $L^{-1}\iint \mu d^2\overline{u}/dz^2\,dx\,dz \approx L^{-1}\int \tau^x/\rho_0\,dx$ (dotted line); (b) the sum of the form stress and wind stress.

4. Vertically integrated momentum balance

a. Zonally averaged balance

The momentum equations are locally dominated by geostrophy: Zonally averaging allows us to consider the vertically integrated net momentum balance for the full Southern Ocean. Since there is no net transport into the system, the Coriolis term, $f\bar{v}$, integrates to zero, and the zonally integrated pressure gradient term is equivalent to $-f\bar{v}_{ag}$ and represents form stress, as discussed in section 2. Figure 1a shows that form stress balances wind stress according to

$$0 \approx \oint\int_{-H}^{0} \frac{1}{\rho_0}\frac{\partial\overline{p}}{\partial x}\,dz\,dx + \oint \frac{\overline{\tau^x}}{\rho_0}\,dx. \qquad (6)$$

The balance agrees with findings from the FRAM model (Killworth and Nanneh 1994; Stevens and Ivchenko 1997). However, while previous studies have focused largely on the zonally unblocked region between 55°

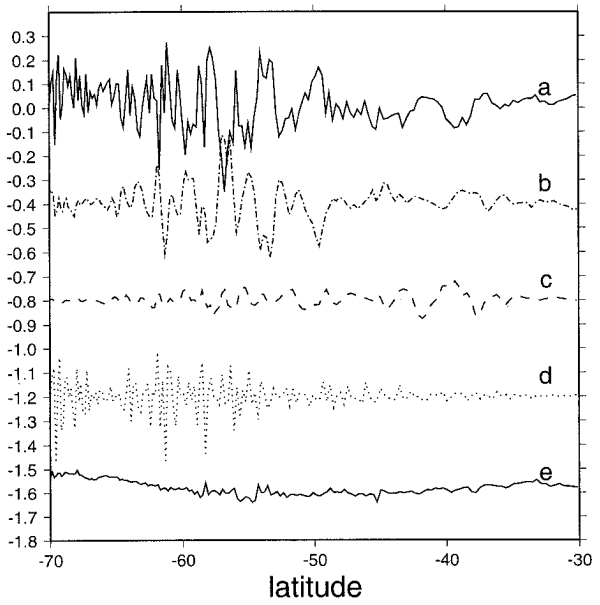

FIG. 2. Vertically integrated and zonally averaged momentum balance in the quarter-degree Semtner–Chervin model output (in $cm^2\ s^{-2}$). Terms shown are (a) the component of form stress not balanced by wind stress ($L^{-1} \iint - \rho_0^{-1}\ \partial\overline{p}/\partial x + \mu\ \partial^2\overline{u}/\partial z^2\ dx\ dz$), (b) the mean equatorward momentum flux divergence ($L^{-1} \iint \partial\overline{u}\ \overline{v}/\partial y\ dx\ dz$), (c) the equatorward eddy flux divergence ($L^{-1} \iint \partial\overline{u'v'}/\partial y\ dx\ dz$), and (d) the biharmonic friction term ($L^{-1} \iint A_m\ \nabla^4\overline{u}\ dx\ dz$). Term (e) represents the residual imbalance. The offset between successive terms is -0.4 $cm^2\ s^{-2}$.

and 62°S, in this analysis latitudes intersected by continents are included since the continents are merely very tall topographic obstructions, which induce form stress in the same way that smaller ridges do. The presence of subsurface topography at even the unblocked latitudes means that the pressure gradient term does not vary dramatically between blocked and unblocked latitudes.

Bottom friction is negligibly small, so that the residual difference between the form stress and the wind stress (Fig. 1b) is an indication of the amount of momentum transferred meridionally rather than vertically. This meridional transfer of momentum links the Southern Ocean with the closed ocean basins to its north. Consider the contribution of each of the terms in the time-averaged momentum equation (1) to this residual momentum balance. The nonnegligible terms, plotted in Fig. 2, are the meridional mean momentum divergence, $\partial\overline{u}\ \overline{v}/\partial y$, the biharmonic friction term, $A_m\ \nabla^4\overline{u}$, and the meridional eddy momentum divergence, $\partial\overline{u'v'}/\partial y$. [Hereafter Cartesian coordinates (x, y) are used for simplicity.] The most significant contribution to the cross-stream momentum balance is due to the mean eddy flux divergence (Fig. 2, line b) and is noticeably larger than the eddy flux divergence from transient eddies (Fig. 2, line c). The remaining terms from Eq. (1) related to the vertical advection of momentum, bottom friction, and long-term velocity tendency are too small to explain the residual momentum imbalance (Fig. 2, line e); instead, the residual is probably due to small errors in the wind field used for this analysis, nonlinearities in the pressure gradient term, nonlinearities in the surface Richardson-number-dependent vertical viscosities, and errors in computing the meridional eddy flux divergence terms.

The overall results are consistent with the findings of Stevens and Ivchenko (1997) for the FRAM model. In the Semtner–Chervin model, biharmonic friction (Fig. 2, line d) appears more substantial than the FRAM results would indicate, but this effect is most noticeable at high latitudes, outside of the FRAM analysis region where friction removes point-to-point spikiness.

The Semtner–Chervin results also qualitatively resemble the quasigeostrophic (QG) channel model results, which showed that stationary eddies were the dominant factor accounting for latitudinal differences between the locations of surface wind forcing and bottom topographic form stress. In a two-layer idealized QG channel model (Wolff et al. 1991), eddy momentum terms were substantially larger than they are in the primitive equation results of Fig. 2, with a peak amplitude about half the peak wind stress, and the stationary eddies acted to intensify the form stress to the narrow latitudinal band of the bathymetric obstruction. In contrast, results of a three-layer QG model with realistic bathymetry (Marshall et al. 1993) showed that stationary eddies behaved much as they do in the Semtner–Chervin model output. In the three-layer model, the mean eddy amplitudes were about an order of magnitude smaller than the wind forcing and did not intensify the form stress to a narrow latitudinal band. The similarity of these three-layer QG results to the Semtner–Chervin output suggests that, in both QG and primitive equation models with realistic bathymetry, form stress can act over a broad latitude range and stationary eddies are only required to transfer momentum short distances between the locations where it is input by wind stress and where it can be removed via form stress.

b. Average balance along streamlines

The zonally averaged momentum balance illustrates how the flow responds to the predominant zonal wind forcing, but it is not the only way to consider the momentum balance. Marshall et al. (1993) argued that properties fluxed northward in one large stationary meander of the ACC will return southward within the ACC, providing no net flux of momentum or other properties along the circumpolar path. To eliminate the effect of standing eddies and to ask what processes control the structure of the mean meandering ACC itself, they advocated studying the momentum balance in stream coordinates; the geostrophic component of the mean cross-stream Coriolis term (fv_g) is zero, and only ageostrophic effects, transient eddies, and frictional effects may act to redistribute momentum across the ACC.

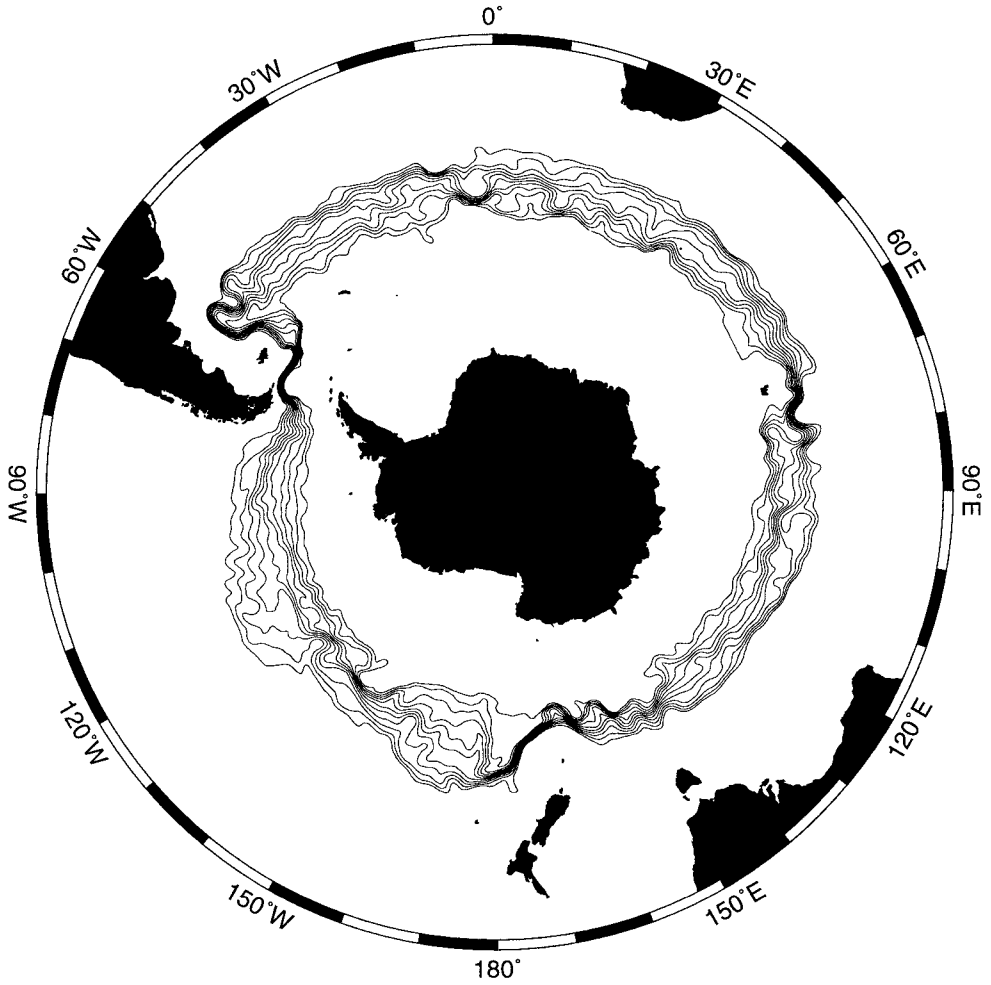

FIG. 3. Sea surface height contours used for mapping vertically integrated momentum balance in stream coordinates. Contours extend from −0.5 m at the south to 0.5 m at the north with a contour interval of 0.1 m.

For vertically averaged flow, there is no easily defined geostrophic contour onto which the equations of motion may be translated. Instead, consider the flow along the sea surface height contours η defined by the model free surface, as shown in Fig. 3. The equations of motion are translated into stream coordinates by first defining continuous height contours, then determining the zonal distance s_x and meridional distance s_y between consecutive points, and finally rotating the equations, using a cosine/sine transformation, so that

$$\text{alongstream momentum} = M_x \times \frac{s_x}{\sqrt{s_x^2 + s_y^2}} + M_y \times \frac{s_y}{\sqrt{s_x^2 + s_y^2}}, \quad (7)$$

where M_x is the x-momentum equation and M_y the y-momentum equation. (Note that curvature terms are not introduced into this expression for alongstream momentum because the advective and frictional terms, which would be altered by the change in coordinates, are computed before converting to alongstream coordinates.) The resulting rotated momentum equation is essentially identical to (1) except that all coordinates are in stream coordinates. Rotated coordinates will be labeled x_s and y_s, the alongstream velocity is u_s, and the cross-stream velocity is v_s.

The dominant momentum balance shown in Fig. 4a is analogous to the zonally averaged balance: the total transport across streamlines integrates to zero; the pressure gradient term, integrated along streamlines, represents the form stress. This form stress provides the dominant balance for wind stress as indicated in Fig. 4a.

The residual difference between wind stress and form stress is substantially different from the zonally averaged case, as shown in Fig. 4b. While mean eddies dominate the zonally averaged balance, in the alongstream average substantial contributions come from a combination of biharmonic friction and transient and mean eddy flux divergences. Marshall et al. (1993) predicted that transient eddies should be critical to the overall balance of the real ocean. However, just as Ivchenko

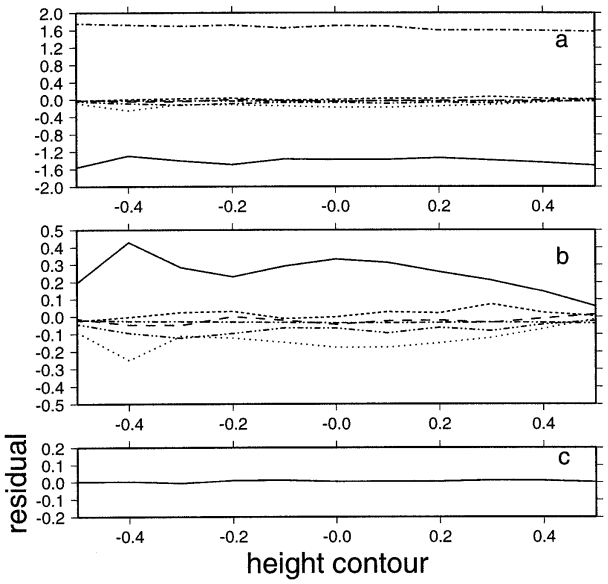

FIG. 4. Momentum balance integrated vertically and averaged along streamlines in the quarter-degree Semtner–Chervin model output (in $cm^2\ s^{-2}$). (a) The (negative) ageostrophic Coriolis term ($L^{-1} \iint f\overline{v} - f\overline{v}_g\ ds\ dz$) rotated into stream coordinates (solid line), the mean wind stress (dash–dot line), the mean equatorward momentum flux divergence $L^{-1} \iint \partial \overline{u}\,\overline{v}/\partial y\ ds\ dz$ (dash double-dotted line), the transient equatorward eddy flux divergence $L^{-1} \iint \partial \overline{u'v'}/\partial y\ ds\ dz$ (long dashed line), the biharmonic friction term $L^{-1} \iint A_m\ \nabla^4 \overline{u}\ ds\ dz$ (dotted line), mean vertical flux divergence (short dashed line), and bottom friction (double-dashed–double-dotted line). (b) The same information, except that the solid line represents the portion of the ageostrophic velocity not accounted for by the wind stress. (c) The residual momentum imbalance when all these terms are summed. If the momentum balance were perfect, this term would be constant at zero. The errors inherent in the along-stream integration are comparable in magnitude to this imbalance.

et al. (1996) found for FRAM, biharmonic friction is the largest of lateral momentum transfer terms in this model. The large magnitude of the biharmonic friction term relative to the transient eddy term indicates that subgrid-scale processes are more important than resolved eddy processes in fluxing momentum across the numerical ACC. Thus the results suggest that the model may not adequately resolve the high wavenumber eddy processes necessary to represent cross-stream momentum transfer.

In addition to biharmonic friction, the remaining terms in the momentum balance are also important. The mean eddy flux term ($\partial \overline{u}_s \overline{v}_s / \partial y_s$) exceeds the transient eddy flux term ($\partial \overline{u_s' v_s'} / \partial y_s$) so that stationary eddies appear more significant than transient eddies. This effect can be attributed to several factors. First, the largest contribution occurs because the surface streamlines used for this analysis are not precisely parallel to the deep geostrophic flow, so we can predict a deep cross-stream geostrophic component to the mean eddy flux term. Second, a large Ekman transport at the surface produces a substantial ageostrophic mean eddy flux. And finally, even if the Reynolds stress terms ($\overline{u}_s \overline{v}_s$) were exactly zero along streamlines, because of the model discretization the Reynolds stress divergences would nonetheless be nonzero in stream coordinates. In addition to the horizontal advective term, the mean vertical momentum flux divergence is nonzero because of the free surface and tends to accelerate the flow. Bottom friction and transient vertical eddy flux divergences are less significant.

c. Local balance along streamlines

Although the global balance is dominated by wind stress and bottom form stress, effects other than these may be substantial portions of the local dynamics along the path of the ACC. The momentum balance along the 0.2-m height contour (fourth from the north in Fig. 3) reveals dramatic shifts in the magnitude of the terms in the momentum balance, as indicated in Fig. 5. Two flow regimes appear: in relatively quiescent regions where the ocean is deep and bathymetry plays a negligible role, such as the region between 10°E and 60°E, the terms in the momentum balance are small and vary gradually over large distances; here the Coriolis term $f v_{ag}$ roughly balances wind stress. In contrast, at three isolated topographic features—Kerguelen Island at 70°E, Macquarie Ridge and Campbell Plateau at 170°E, and Drake Passage at 60°W—the terms are larger and more variable, and eddy fluxes and friction may be substantially larger than the wind stress. All of these topographic features extend to the ocean surface in certain locations, but are deeper than 1000 m through the central portion of the ACC flow. Their presence has a dramatic effect on the magnitude of the terms in the momentum balance.

The difference between regions near topography and deep midbasin areas can be represented statistically by measuring the percentage of alongstream points at which at least 50% of the ageostrophic Coriolis term ($f v_{ag}$, the solid line in Fig. 5a) is locally explained by the wind (dotted line in Fig. 5a): This is true at 81% of points in quiescent regions, but at just 30% of points in eddy active regions. In other words, the wind is fairly constant along streamlines; in quiescent regions, the ageostrophic surface Ekman transport locally balances the wind. In regions with strong topographic variations, the ageostrophic velocity, the mean and transient horizontal flux divergences, the mean vertical flux divergence, and horizontal viscosity all substantially contribute to the overall momentum balance.

These differences might imply that the ACC dynamics near topographic features are substantially altered from those in broad ocean basins. To examine the relative importance of momentum flux divergences and friction in the alongstream momentum balance, each of the terms is compared with the residual difference between the wind stress and ageostrophic Coriolis term. Although the magnitudes of fluctuations of each of the terms in Fig. 5 differ dramatically between quiescent

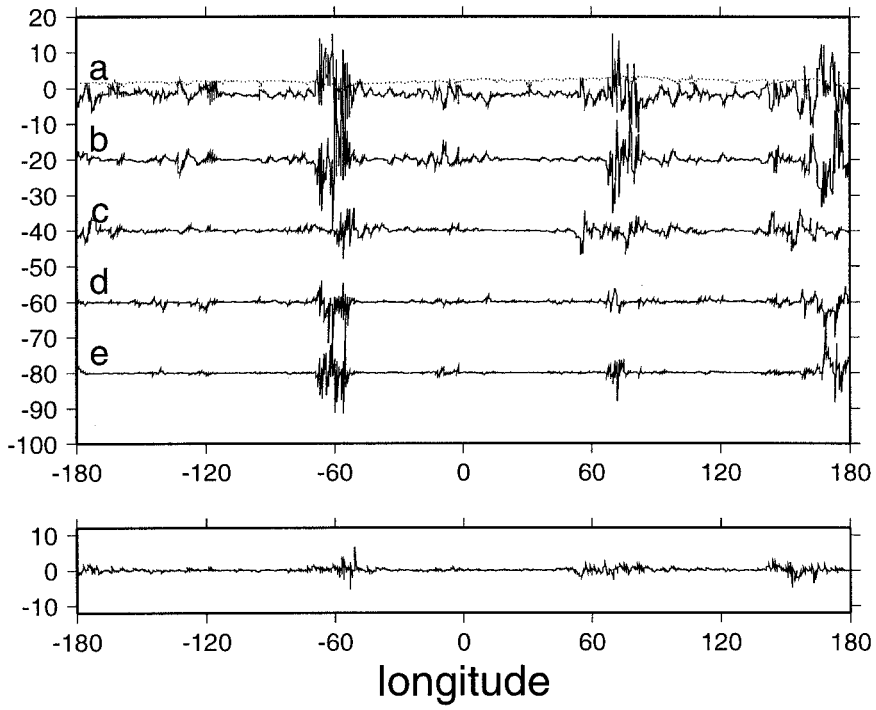

FIG. 5. Vertically integrated momentum balance along the height contour 0.2 in the quarter-degree Semtner–Chervin model output (in cm^2 s^{-2}). Upper panel shows (a) the ageostrophic Coriolis term, $\int f v_{ag} dz$, and (dashed) wind stress; (b) the equatorward mean momentum flux divergence; (c) the equatorward eddy flux divergence; (d) the biharmonic friction; and (e) mean vertical eddy fluxes; terms are offset by -20. The lower panel shows the residual imbalance, which is due to inaccuracies in computing the pressure gradient and eddy flux terms and acceleration due to curvature of the ACC path.

regions and energetic regions, the actual partitioning of energy between frictional and nonlinear terms varies less substantially. Table 1 indicates a slight decrease in the importance of transient eddy fluxes and an increase in the importance of the mean vertical momentum flux divergence within eddy-active regions, but the differences account for less than 10% of the variability. Thus the overall dynamical regime does not shift enormously between eddy-active and quiescent regions, and the major difference appears to be the substantially greater spatial variability in the momentum balance terms, corresponding to increased kinetic energy in eddy-active regions. Energy levels along streamlines will be addressed in greater detail in section 5.

TABLE 1. The contribution of each major term (in percent) in the vertically integrated, time-averaged alongstream momentum equation. Values shown indicate the percentage of points alongstream at which the indicated term accounts for over 50% of the residual difference between the ageostrophic Coriolis term fv_{ag} and wind stress, that is, points where $|(fv_{ag} - \text{wind stress} - \text{term})/(fv_{ag} - \text{wind stress})| < 0.5$. Eddy active regions correspond to three topographic features: Kerguelen Island (76° to 82°E), Campbell Plateau (145° and 170°E), and Drake Passage (70° to 45°W). This statistical comparison, while unusual, effectively minimizes the impact of large outliers. The number of points at the bottom indicates the total number of alongstream values considered in each category.

Term	All points	Eddy active regions	Quiescent regions
$\partial \overline{u}\,\overline{v}/\partial y$	53	56	52
$\partial \overline{u'v'}/\partial y$	35	29	36
$A_m \nabla^4 \overline{u}$	19	20	19
$\partial \overline{u}\,\overline{w}/\partial z$	11	16	10
Number of points	16 313	3601	12 701

d. Form stress along streamlines

Because the ageostrophic velocity term does not precisely represent form stress except in a vertically and circumpolarly integrated sense, form stress will instead be computed directly from the pressure gradient term in order to look at its regional influence. In this case, the pressure effects on the boundary of the region must be removed, leaving only the pressure difference due to ridges within the study region. Thus the vertically integrated form stress is the difference between the geostrophic transport predicted from the pressure values on the region boundaries and the actual geostrophic transport through the region;

$$\text{form stress} = \frac{1}{\rho_0}\int_{-H}^{0} (p_f - p_i)\, dz - \frac{1}{\rho_0}\int_0^L \int_{-H}^{0} \frac{\partial p}{\partial x}\, dz\, dx, \quad (8)$$

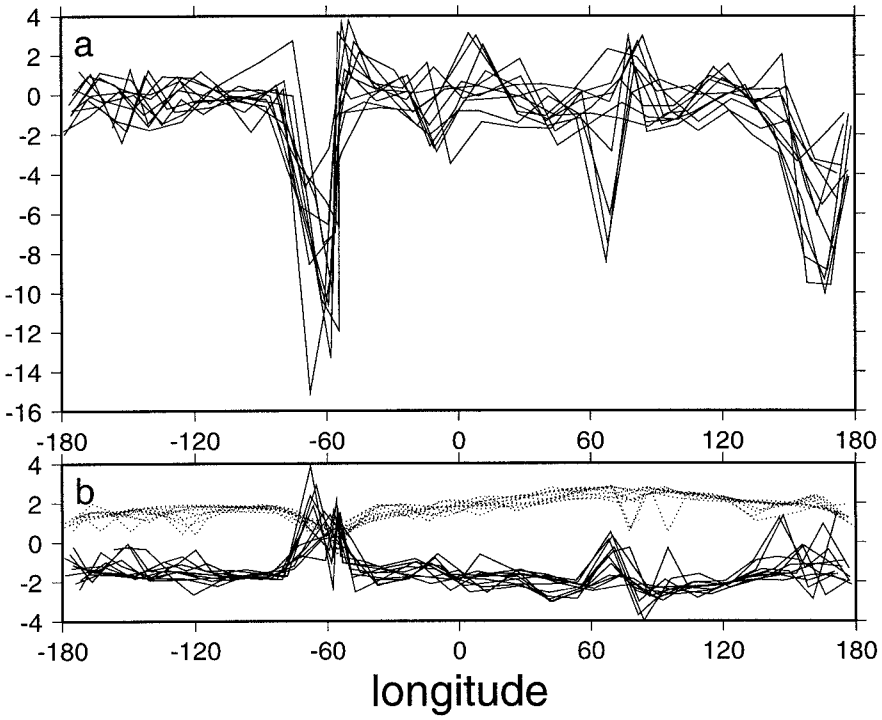

FIG. 6. (a) Total vertically integrated form stress [as defined in (8)], integrated along roughly 10° wide swaths along streamlines in the ACC and divided by the length of the streamlines (in $cm^2\ s^{-2}$). This provides a measure of the portion of form stress (averaged along streamlines) generated in each longitude region. Results for all height contours from −0.5 to 0.5 m, as shown in Fig. 3, are superimposed. (b) Wind stress (dashed line) and ageostrophic velocity (solid line) for the same segments used in (a) indicate that the wind stress is fairly uniform, even though the actual form stress itself is concentrated at three ridges.

where p_i is the westernmost pressure in the basin at a given latitude and depth, p_f is the easternmost pressure, and 0 and L correspond to the western and eastern limits of a two-dimensional region. Thus the pressure $p_i(z) = p(x = 0, z)$ for all depths above the ocean floor at $x = 0$. Below the ocean floor at $x = 0$, $p_i(z)$ is equal to the westernmost bottom pressure measurement within the region. Similarly $p_f = p(L, z)$ except at levels below the ocean floor at $x = L$.

Although wind forcing is uniformly balanced by the ageostrophic portion of the Coriolis term along streamlines, the actual form stress is caused by individual ridges. Using (8), the effective form stress is estimated over roughly 10° swaths in longitude. The results, illustrated in Fig. 6, indicate that form stress can be attributed almost exclusively to three major topographic features: Drake Passage near 70°W, Kerguelen Island near 60°E, and Campbell Plateau around 170°E. Smaller topographic features are not an apparent source of form stress in the numerical model output.

These results are consistent with analytic results by Wang and Huang (1995) who found that in order to influence the net ACC transport ridges must exceed a critical height, which depends on the channel width, depth, and the size of β. Similarly, in a quasigeostrophic model, Treguier and McWilliams (1990) found that wider ridges were important sources of form stress, while smaller features had much less influence on the overall momentum balance. While these two idealized models may not accurately represent the ACC along most of its trajectory, each of the three topographic features that are sources of form stress in the Semtner–Chervin model are quite tall, breaching the surface in some locations, and they do confine the ACC to a narrow channel. Thus, the numerical model may respond to the same constraints as the idealized models.

In contrast to the form stress' localized response to three ridges, the ageostrophic velocity term shown in Fig. 6b responds uniformly to the wind. It does not represent the form stress except when averaged around the entire circumpolar path and may be a misleading proxy for form stress.

5. Surface kinetic energy

Now armed with some knowledge of how the model momentum balance functions, we can consider how the model compares with the the ocean. The Geosat altimeter, which flew in an exact repeat mission from October 1986 to December 1989, provided repeated measurements of sea surface height variability from which surface eddy kinetic energy can be estimated. Increased

eddy kinetic energy near topographic features may be a result of topographic lee waves and may feed greater instabilities, but as section 4c has shown, it does not appear to alter the overall momentum balance. Since the major alongstream variations in the momentum balance appear to be in the amplitude of the fluctuations rather than in the actual partitioning of momentum between the terms, changes in energy serve as a convenient indicator of the major momentum variations for comparison with other measurements. Eddy kinetic energy has the advantage that in addition to being easily computed from model output, it may also be estimated from altimeter data.

Detailed analyses by Morrow et al. (1992) and Johnson et al. (1992) have used crossover techniques for estimating eddy kinetic energy and Reynolds stresses from altimeter data. Here, a slightly different methodology has been developed. Rather than confining investigation to crossover points and temporally interpolating to match ascending and descending measurements, the alongtrack variability data were objectively mapped using decorrelation scales estimated directly from the data (Gille and Kelly 1996). The resulting regularly gridded instantaneous sea surface height maps include error estimates (Gille 1995). Eddy kinetic energy and Reynolds stress estimates computed from the gridded data are generally consistent with the results of Morrow et al. (1992).

Numerical models have historically tended to underestimate surface kinetic energy relative to altimeter measurements. Wilkin and Morrow (1994) found that, on average, surface eddy kinetic energies estimated from the altimeter were a factor of 6 greater than those computed by the half-degree model. In contrast, in this analysis, the discrepancy is reduced to a factor of 2, suggesting that the finer resolution of the quarter-degree model more effectively represents eddy processes. Between 45° and 60°S, the mean eddy kinetic energy measured by the altimeter is 1.5×10^{-2} m^2 s^{-2}, compared with 7.2×10^{-3} m^2 s^{-2} in the model output. Eddy kinetic energy is greatest along the axis of the ACC. In these energetic regions, Wilkin and Morrow (1994) found closer agreement, with the ratio of altimeter to model eddy kinetic energy reduced to between 2.2 and 4. In this analysis, eddy kinetic energy has been averaged along mean surface streamlines, determined from the altimeter data by Gille (1994). The results are similar to those of Wilkin and Morrow: averaged along streamlines, eddy kinetic energy measured by the altimeter is about 1.6 times greater than that found in the model, as indicated in Fig. 7. Like the FRAM model results shown by Ivchenko et al. (1996, Fig. 8), the Semtner–Chervin model indicates a linear increase in eddy kinetic energy with sea surface height, but this model is roughly twice as energetic as FRAM. Neither model captures the eddy kinetic energy peak seen by the altimeter at the 0.1-m height contour, but the differences may be due to the broader nature of the ACC in portions of the model

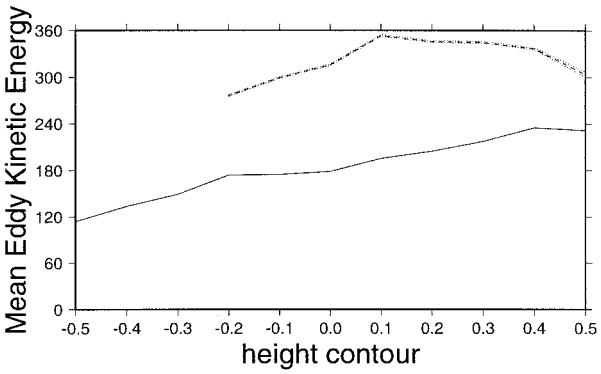

FIG. 7. Eddy kinetic energy averaged along surface height contours. Solid line indicates energy in the quarter-degree Semtner–Chervin model output (in cm^2 s^{-2}). Dashed line is the same quantity in altimeter data, with error limits indicated by dotted lines.

output. This peak in eddy kinetic energy near the axis of the Subantarctic Front (SAF) suggests that the meandering ACC fronts themselves may account for a substantial portion of eddy kinetic energy in the Southern Ocean.

The results of the alongstream momentum balance in section 4c show that eddy kinetic energy varies substantially along streamlines, as shown in Fig. 8. In the numerical model output, eddy kinetic energy has a relatively small background value and peaks at three major locations associated with topographic obstruction of the flow: Drake Passage (60°W), Kerguelen Plateau (70°E), and Campbell Plateau (170°E). These kinetic energy peaks may be due to topographic lee waves associated with isopycnal displacements caused by form drag. Energy levels measured by the altimeter are relatively low in quiescent deep ocean areas, but rise dramatically at topographic features. However, unlike the model results, which suggest that only three topographic features are important in the momentum balance, the altimeter data show a broader energy peak at Drake Passage (60°W) and increased energy near the Crozet Plateau (40°E) and at the Eltanin and Udintsev Fracture Zones in the central Pacific (140°W). The northern side of the ACC also shows increased energy near 140°E, where the SAF crosses over the Indian–Antarctic Ridge. Thus, in addition to the three major topographic features that increase eddy kinetic energy in the model, several additional ridge structures are also sources of increased eddy kinetic energy. The larger background level could be attributed to instrument noise, as well as to eddy variability unresolved by the model.

While eddy kinetic energy is an indicator of heightened eddy variability, mean kinetic energy is an indicator of the strength of the mean flow. Mean kinetic energy along streamlines (Fig. 9) in the numerical model output has a background level very close to zero but surges upward near the three major topographic features at Drake Passage, Kerguelen Island, and Campbell Plateau, where streamlines compress together akin to a

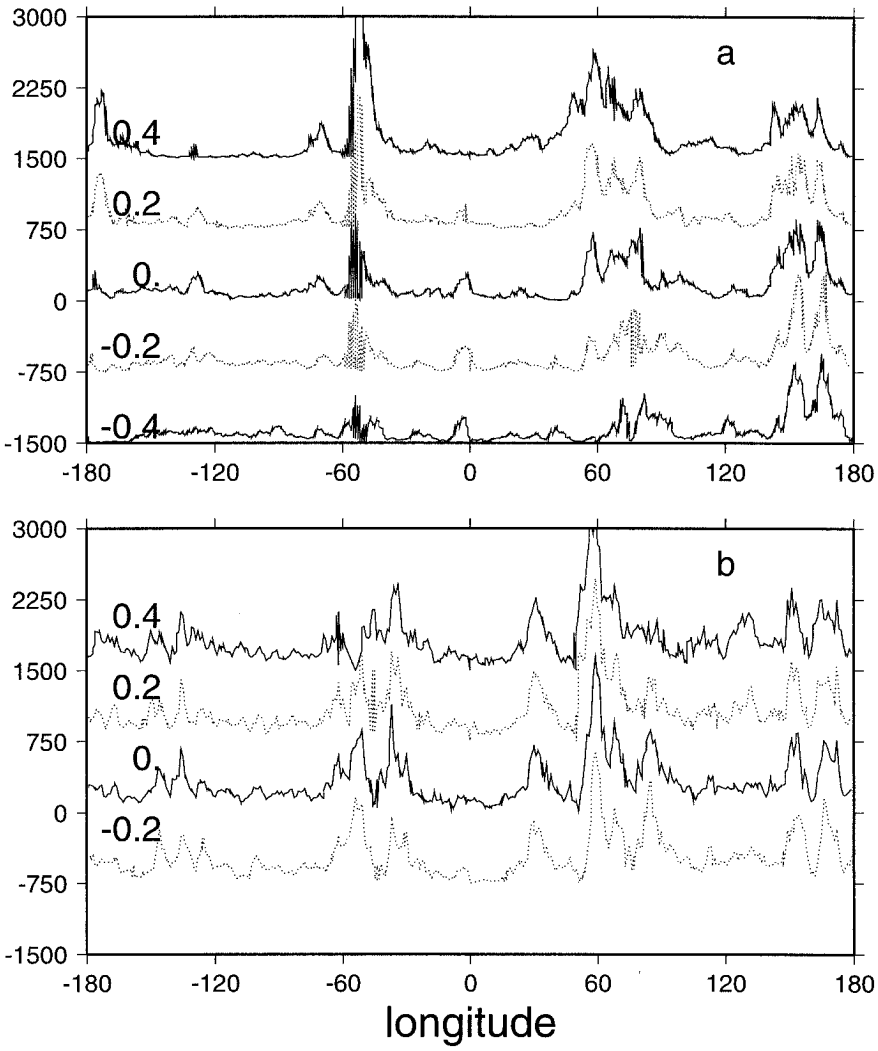

FIG. 8. Eddy kinetic energy along surface height contours. (a) Energy for the quarter-degree Semtner–Chervin model output in $cm^2\ s^{-2}$, along height contours corresponding to -0.4, -0.2, 0, 0.2, and 0.4 m. (b) Eddy energy along height contours in Geosat altimeter data, for contours -0.2, 0, 0.2, and 0.4 m. Error estimates obtained from the objective mapping procedure for the altimeter measurements average 50 $cm^2\ s^{-2}$. Lines are offset by 750 $cm^2\ s^{-2}$.

western boundary current. Model mean kinetic energy levels also fluctuate in the mid-Atlantic and mid-Pacific Oceans. In the altimeter data, mean kinetic energy is calculated based on the reconstructed mean sea surface height field of Gille (1994). The altimetric mean kinetic energy rises above its background level in the same locations as does the model energy. However, the altimeter results show less dramatic variations in energy levels; mean kinetic energy does not rise as high at major topographic features nor does it reduce as smoothly to low background levels in mid ocean.

Assuming that kinetic energy in the Southern Ocean is largely associated with topographically generated stationary and transient features, the observed energy differences may indicate that many more than three topographic features significantly influence ACC dynamics. The greater impact of topography in the observed ocean relative to the model might be attributed to one of several related factors. First, it may indicate that subsurface topographic features in the ocean define narrow deep ocean channels that are better able to support deep frictional boundary currents than the coarse topography of the numerical model. Second, it may mean that the model has too much horizontal diffusion of momentum and tracers and not enough along-isopycnal diffusion so that momentum transfer along isopycnals is inhibited. Third, it may simply be a manifestation of small vertical velocities in the model related to coarse vertical resolution, unrealistic deep density fields, or the unusual thermodynamics imposed by the surface boundary condition represented through relaxation of upper-level temperature and salinity to Levitus. Fourth, it may in-

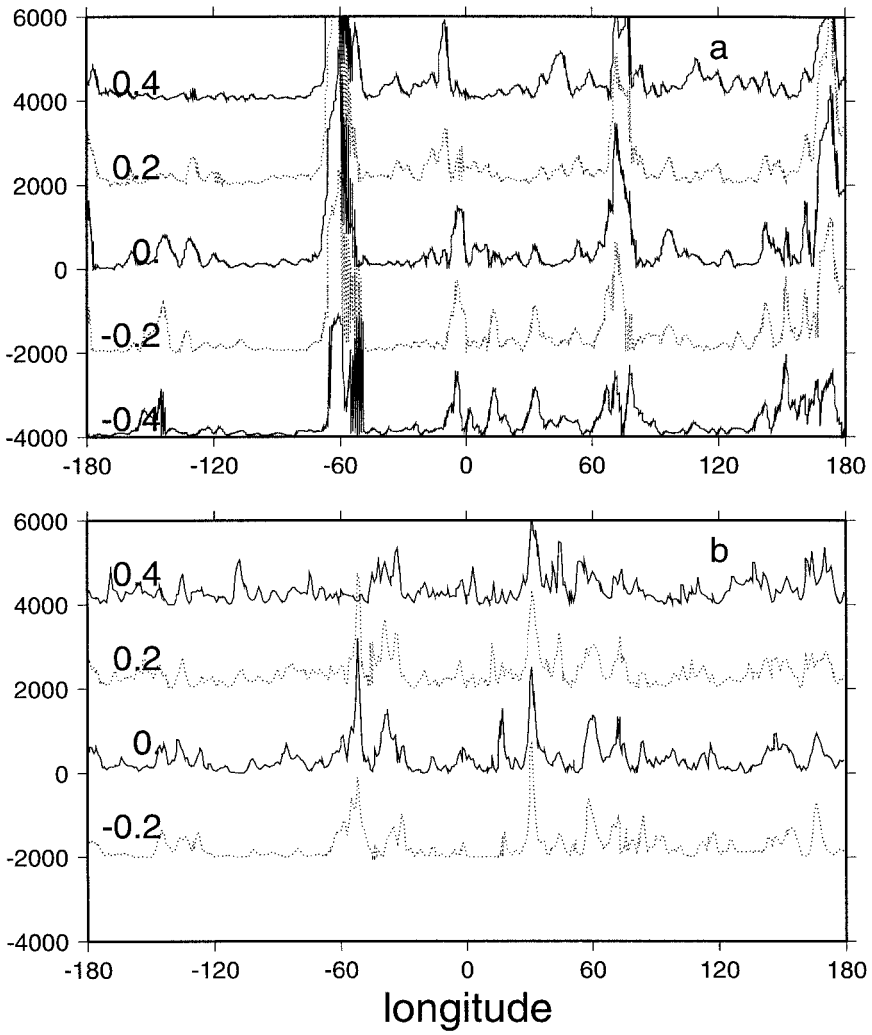

FIG. 9. Mean kinetic energy along surface height contours. (a) Energy for the quarter-degree Semtner–Chervin model output (in $cm^2\ s^{-2}$) along height contours corresponding to -0.4, -0.2, 0.0, 0.2, and 0.4 m. (b) Mean energy along height contours in Geosat altimeter data, for contours -0.2, 0.0, 0.2, and 0.4 m. Average error is 160 $cm^2\ s^{-2}$. Offset between lines is 2000 $cm^2\ s^{-2}$.

dicate that the model's 33.5-yr initialization period is not sufficiently long for higher-order baroclinic modes initially injected into the system to spin down. The barotropic mode has a timescale of 12 days and is likely to be well represented by the model. However, the first baroclinic mode, with 40-km Rossby radius, has a 140-yr timescale that is unlikely to be captured in this model run.

Regardless of the specific physical processes at work, the fact that only topographic features that breach the surface are sources of form stress and heightened eddy or mean kinetic energy in the model suggests that communication between the deep ocean and the surface is greater in the real ocean than in the model so that deeper topographic features have a greater impact on ocean circulation. This difference may explain why the model transport is 50% larger than the observed Southern Ocean transport.

6. Summary

This combination of numerical model output and altimeter data used for this investigation has elucidated several key features of the Southern Ocean momentum balance.

The momentum balance has been examined by averaging zonally, by averaging along stream coordinates, and by examining the alongstream variations of the momentum balance. Consistent with previous studies, the vertically averaged balance shows that form stress balances wind stress, both in zonal coordinates and in stream coordinates. In zonally averaged coordinates, the

residual difference between wind stress and form stress is predominantly balanced by horizontal mean momentum flux divergences while biharmonic friction and eddy flux divergences play a less important role. Averaging along streamlines diminishes the role of the mean flux divergences since the cross-stream mean geostrophic velocity is zero. Instead, biharmonic friction is the largest term balancing the form stress divergence.

Horizontal viscosity is a parameterization of subgrid-scale processes; if the magnitude of the terms in these results is representative of real ocean processes, then either the model resolution is inadequate or a more physically justified representation of eddy viscosity should be found. The magnitude of horizontal viscosity suggests that the dominant scales of motion are smaller than the grid spacing or, alternatively, that the particular parameterization used in the model is inadequate, implying that a smaller viscosity coefficient or an isopycnal formulation for viscosity might yield better results. Both explanations indicate the importance of parameterizing subgrid-scale processes correctly.

The alongstream momentum balance shows substantial variability associated with three large topographic features: Drake Passage, Kerguelen Island, and Campbell Plateau. At each of these, land intersects the path of the ACC, and essentially all form stress is due to these three features. Despite the variability, the relative importance of terms in the momentum balance does not change substantially between regions associated with topographic barriers and quiescent midbasin regions. The major differences appear to be in the kinetic energy level rather than the structure of the dynamical balance. Given this observation, eddy kinetic energy has been examined along streamlines in the numerical model and in the altimeter measurements.

Both model and data feature narrow meandering jets that make up the ACC, and energy levels are greatest along the jet axes. Overall the altimeter data indicate twice as much eddy kinetic energy as the model output predicts. This difference, coupled with the surprising importance of horizontal viscosity in the model, suggests that the model resolution may not be sufficient to capture all eddy processes. Along surface streamlines model eddy kinetic energy shows three substantial peaks corresponding to the three major topographic features, all of which extend through the entire water column. In the altimeter measurements, eddy kinetic energy peaks at these same locations, but also at many smaller topographic features, indicating that minor ridges may also be sources of form stress.

The resemblances between model and oceanic jet structures and the order of magnitude agreement in energy levels together suggest that the numerical model captures upper-ocean physics reasonably well. Discrepancies between model and measurements offer additional insight into the critical dynamics governing the ACC and suggest that the baroclinic structure of the model may not duplicate oceanic processes.

Acknowledgments. Many thanks to Bert Semtner and Bob Chervin who made their model results readily available and to Tony Craig and Robin Tokmakian who helped in extracting and interpreting the data. This study benefited from discussions with Kathie Kelly, Mike McCartney, John Marshall, John Toole, and Terry Joyce. Comments from the anonymous reviewers, Greg Holloway, and Stefan Llewellyn Smith have helped to improve the manuscript. This work was supported by National Aeronautics and Space Administration Contract NAGW-1666 and by NOAA Award NA47GP0188 to the Lamont/Scripps Consortium for Climate Research.

REFERENCES

Bryden, H. L., and R. A. Heath, 1985: Energetic eddies at the northern edge of the Antarctic Circumpolar Current in the southwest Pacific. *Progress in Oceanography,* Vol. 14, Pergamon, 65–87.

FRAM Group, 1991: An eddy-resolving model of the Southern Ocean. *Eos, Trans. Amer. Geophys. Union,* **72,** 169–175.

Gill, A. E., 1968: A linear model of the Antarctic Circumpolar Current. *J. Fluid Mech.,* **32,** 465–488.

Gille, S. T., 1994: Mean sea surface height of the Antarctic Circumpolar Current from GEOSAT data: Method and application. *J. Geophys. Res.,* **99,** 18 255–18 273.

——, 1995: Dynamics of the Antarctic Circumpolar Current: Evidence for topographic effects from altimeter data and numerical model output. Ph.D. thesis, MIT/Woods Hole Oceanographic Institution Joint Program, 216 pp. [Available from Woods Hole Oceanographic Institution, Woods Hole, MA 02543.]

——, and K. A. Kelly, 1996: Scales of spatial and temporal variability in the Southern Ocean. *J. Geophys. Res.,* **101,** 8759–8773.

Houry, S., E. Dombrowsky, P. DeMey, and J.-F. Minster, 1987: Brunt–Väisälä frequency and Rossby radii in the South Atlantic. *J. Phys. Oceangr.,* **17,** 1619–1626.

Ivchenko, V. O., K. J. Richards, and D. P. Stevens, 1996: The dynamics of the Antarctic Circumpolar Current. *J. Phys. Oceanogr.,* **26,** 753–774.

Jayne, S. R., and R. Tokmakian, 1997: On the forcing and sampling of ocean general circulation models: Impact of high-frequency motions. *J. Phys. Oceanogr.,* **27,** 1173–1179.

Johnson, G. C., and H. L. Bryden, 1989: On the size of the Antarctic Circumpolar Current. *Deep-Sea Res.,* **36,** 39–53.

——, R. H. Stewart, C. K. Shum, and B. D. Tapley, 1992: Distribution of Reynolds stress carried by mesoscale variability in the Antarctic Circumpolar Current. *Geophys. Res. Lett.,* **19,** 1201–1204.

Killworth, P. D., and M. M. Nanneh, 1994: Isopycnal momentum budget of the Antarctic Circumpolar Current in the Fine Resolution Antarctic Model. *J. Phys. Oceanogr.,* **24,** 1201–1223.

——, D. Stainforth, D. J. Webb, and S. M. Paterson, 1991: The development of a free-surface Bryan–Cox–Semtner ocean model. *J. Phys. Oceanogr.,* **21,** 1331–1348.

Levitus, S., 1982: *Climatological Atlas of the World Oceans.* NOAA Prof. Paper No. 13, U.S. Govt. Printing Office, 173 pp plus microfiche.

Marshall, J., D. Olbers, H. Ross, and D. Wolf-Gladrow, 1993: Potential vorticity constraints on the dynamics and hydrography of the Southern Ocean. *J. Phys. Oceanogr.,* **23,** 465–487.

McWilliams, J. C., W. R. Holland, and J. H. S. Chow, 1978: A description of numerical Antarctic Circumpolar Currents. *Dyn. Atmos. Oceans,* **2,** 213–291.

Morrow, R., J. Church, R. Coleman, D. Chelton, and N. White, 1992: Eddy momentum flux and its contribution to the Southern Ocean momentum balance. *Nature,* **357,** 482–484.

Munk, W. H., and E. Palmén, 1951: Note on the dynamics of the Antarctic Circumpolar Current. *Tellus,* **3,** 53–55.

Orsi, A. H., T. Whitworth III, and W. D. Nowlin Jr., 1995: On the

meridional extent and fronts of the Antarctic Circumpolar Current. *Deep-Sea Res. I,* **42,** 641–673.

Pacanowski, R. C., and S. G. H. Philander, 1981: Parameterization of vertical mixing in numerical models of tropical oceans. *J. Phys. Oceanogr.*, **11,** 1443–1451.

Semtner, A. J., 1986: Finite-difference formulation of a world ocean model. *Proc of the NATO Advanced Physical Oceanographic Numerical Modelling,* J. J. O'Brien, Ed., Reidel, 187–202.

——, and R. M. Chervin, 1992: Ocean general circulation from a global eddy-resolving model. *J. Geophys. Res.*, **97,** 5493–5550.

Stammer, D., R. Tokmakian, A. Semtner, and C. Wunsch, 1996: How well does a ¼° global circulation model circulation model simulate large-scale oceanic observations? *J. Geophys. Res.*, **101,** 25 779–25 811.

Stevens, D. P., and V. O. Ivchenko, 1997: The zonal momentum balance in a realistic eddy resolving general circulation model of the Southern Ocean. *Quart. J. Roy. Meteor. Soc.*, **123,** 929–951.

Treguier, A. M., and J. C. McWilliams, 1990: Topographic influences on wind-driven stratified flow in a β-plane channel: An idealized model for the Antarctic Circumpolar Current. *J. Phys. Oceanogr.*, **20,** 321–343.

Trenberth, K. E., J. G. Olson, and W. G. Large, 1989: A global ocean wind stress climatology based on ECMWF analyses. NCAR Tech. Rep. NCAR/TN-338+STR, 93 pp. [Available from National Center for Atmospheric Research, P.O. Box 3000, Boulder, CO 80307.]

Wang, L., and R. X. Huang, 1995: A linear homogenous model of wind-driven circulation in a β-plane channel. *J. Phys. Oceanogr.*, **25,** 587–603.

Wilkin, J. L., and R. A. Morrow, 1994: Eddy kinetic energy and momentum flux in the Southern Ocean: Comparison of a global eddy-resolving model with altimeter, drifter, and current-meter data. *J. Geophys. Res.*, **99,** 7903–7916.

Wolff, J.-O., E. Maier-Reimer, and D. J. Olbers, 1991: Wind-driven flow over topography in a zonal β-plane channel: A quasi-geostrophic model of the Antarctic Circumpolar Current. *J. Phys. Oceanogr.*, **21,** 236–264.